Tectonophysics 880 (2024) 230332

Contents lists available at ScienceDirect

Tectonophysics

journal homepage: www.elsevier.com/locate/tecto

Brittle sedimentary strata focus a multimodal depth distribution of seismicity during hydraulic fracturing in the Sichuan Basin, Southwest China

Mengke An [a,b], Derek Elsworth [b,c], Fengshou Zhang [d,*], Rui Huang [d], Junlun Li [e], Zhengyu Xu [f], Zhen Zhong [g], Manchao He [h]

[a] Department of Civil and Environmental Engineering, The Hong Kong Polytechnic University, Hung Hom, Kowloon, Hong Kong 100872, China
[b] Department of Energy and Mineral Engineering, EMS Energy Institute and G3 Center, The Pennsylvania State University, University Park, PA 16802, USA
[c] Department of Geosciences, The Pennsylvania State University, University Park, PA 16802, USA
[d] Department of Geotechnical Engineering, College of Civil Engineering, Tongji University, Shanghai 200092, China
[e] Laboratory of Seismology and Physics of Earth's Interior, School of Earth and Space Sciences, University of Science and Technology of China, Hefei 230026, China
[f] PetroChina Hangzhou Institute of Geology, Hangzhou 310023, China
[g] School of Civil Engineering, Shaoxing University, Shaoxing 312000, China
[h] State Key Laboratory for Geomechanics and Deep Underground Engineering, China University of Mining and Technology, Beijing, China

ARTICLE INFO

Keywords:
Induced seismicity
Hydraulic fracturing
Multimodal earthquake distribution
Fluid diffusion
Poroelastic stress transfer
Brittle sedimentary layers

ABSTRACT

The number of background earthquakes ($M_L \geq 0$) in the southern Sichuan basin, southwest China, has increased thirtyfold as a result of hydraulic fracturing. Background events are originally deep (4–6 *km*) within the sedimentary section but build into a multimodal distribution both at depth and in the shallow stimulated reservoir (2–4 *km*) - representing a counterpoint to the usual triggering of seismicity on deep sub-reservoir basement faults. Surprisingly, the largest events ($M_L \geq 3$) evolve in the deep sedimentary strata (4–6 *km*) that are hydraulically isolated from the injection zone (2–4 *km*) by low permeability layers. We evaluate the friction-stability rheology of the strata within the full stratigraphic section to define the feasibility of nucleation within these shallow and deep strata. These show velocity-neutral to velocity-weakening behavior in the shallow reservoir transitioning to more strongly velocity-weakening with increase in both depth and temperature. Poroelastic stress calculations confirms that stress transfer, rather than transmitted fluid pressures, are capable of directly reactivating critically-stressed faults at depth, with fluid pressures the triggering source within the shallow reservoir.

1. Introduction

Seismicity correlated with hydraulic fracturing (HF) has attracted worldwide attention during industrial-scale injection of fluids, including the stimulation of shale oil/gas, enhanced geothermal systems (EGS), and wastewater disposal (Shapiro et al., 2006; Majer et al., 2007; Ellsworth, 2013; Walsh and Zoback, 2015; Elsworth et al., 2016; Grigoli et al., 2018; Kolawole et al., 2019; Moein et al., 2023). Understanding the physical mechanisms of these anthropogenic earthquakes could help reducing the hazards o large and damaging earthquakes and ensure the safety exploitation of deep energy and resources. The Sichuan Basin in southwestern China (Fig. 1a) hosts rich shale gas resources with current annual production reaching ~20 billion m^3 - representing the most promising shale gas basin in China and the second largest shale gas production area in the world (Qiu et al., 2020; Zou et al., 2020). However, swarms of small to medium-sized earthquakes have occurred in the shale gas demonstration zones of the Sichuan Basin since the introduction of systematic hydraulic fracturing in 2014 (Lei et al., 2017; Meng et al., 2019; Liu and Zahradník, 2020). Moreover, the M_L (local magnitude) 5.7 Xingwen earthquake on December 16, 2018 and M_L 5.3 Gongxian earthquake on January 3, 2019 in the Sichuan basin have been regarded as the largest hydraulic fracturing-induced events around the world (Lei et al., 2019; Atkinson et al., 2020). Given the high population density in this area and recent reports of severe damage and some casualties, clarifying the underlying mechanisms responsible for the hydraulic fracturing-related earthquakes is of great importance.

The Sichuan Basin (Fig. 1a) is a tectonically stable region characterized by a northwestern uplift zone and depressions in the remaining

* Corresponding author.
E-mail address: fengshou.zhang@tongji.edu.cn (F. Zhang).

https://doi.org/10.1016/j.tecto.2024.230332
Received 29 January 2024; Received in revised form 8 April 2024; Accepted 25 April 2024
Available online 26 April 2024

zones. The basin is surrounded by the Qinling-Dabie Orogenic Belt to the north and Jiangnan-Xuefengshan Thrust Belt to the west. The northwest and southwest boundaries correspond to the Longmenshan and Sanjiang Orogenic Belts, respectively. Among the several shale gas demonstration blocks in the Sichuan basin, the Changning Block, extending over the counties of Changning, Gongxian, Xingwen and Junlian, shows the highest level of seismicity. Horizontal well drilling in the Changning Block began in 2011, but systematic hydraulic fracturing for shale gas extraction in this area was initiated only in 2014 (Lei et al., 2017). According to the Chinese national seismic network (CNSN, blue squares in Fig. 1b), the total number of $M_L \geq 0$ earthquakes from January 2009 to June 2021 in Changning Block exceeds 26,000 (red circles in Fig. 1b) with >30 earthquakes having magnitudes (M_L) $\geq$ 4.0 in the zone bounded by N27.5°-29° and E104°-105.5°. The Changning Block represents a marine-terrestrial environment of Neoproterozoic-Paleozoic-Mesozoic age (Table S1 in the supporting information) with Triassic, Permian and Silurian strata widely distributed in the surface outcrops (Fig. 1c). Earthquake swarms are distributed extensively around the Changning Anticline and Jianwu Syncline. The number of $M_L \geq 0$ earthquakes in each quarter year increased from <100 in 2009–2010, to ~100–400 in 2011–2016, to ~400–900 in 2017–2018 and then to >1000 in 2019–2021 (Fig. 1d and Table S2) - representing a strong correlation between the increase in earthquake frequency and hydraulic fracturing. More specifically, the highest number of $M_L \geq 0$ earthquakes is larger than 3000 in the second quarter of 2019, proving a thirtyfold increase of seismicity pre-hydraulic fracturing to *syn*- and post-hydraulic fracturing.

The permanent Chinese national seismic network has limited capacity to accurately characterize the regional seismic events due to both incomplete calibration and sparse coverage with distant interstation

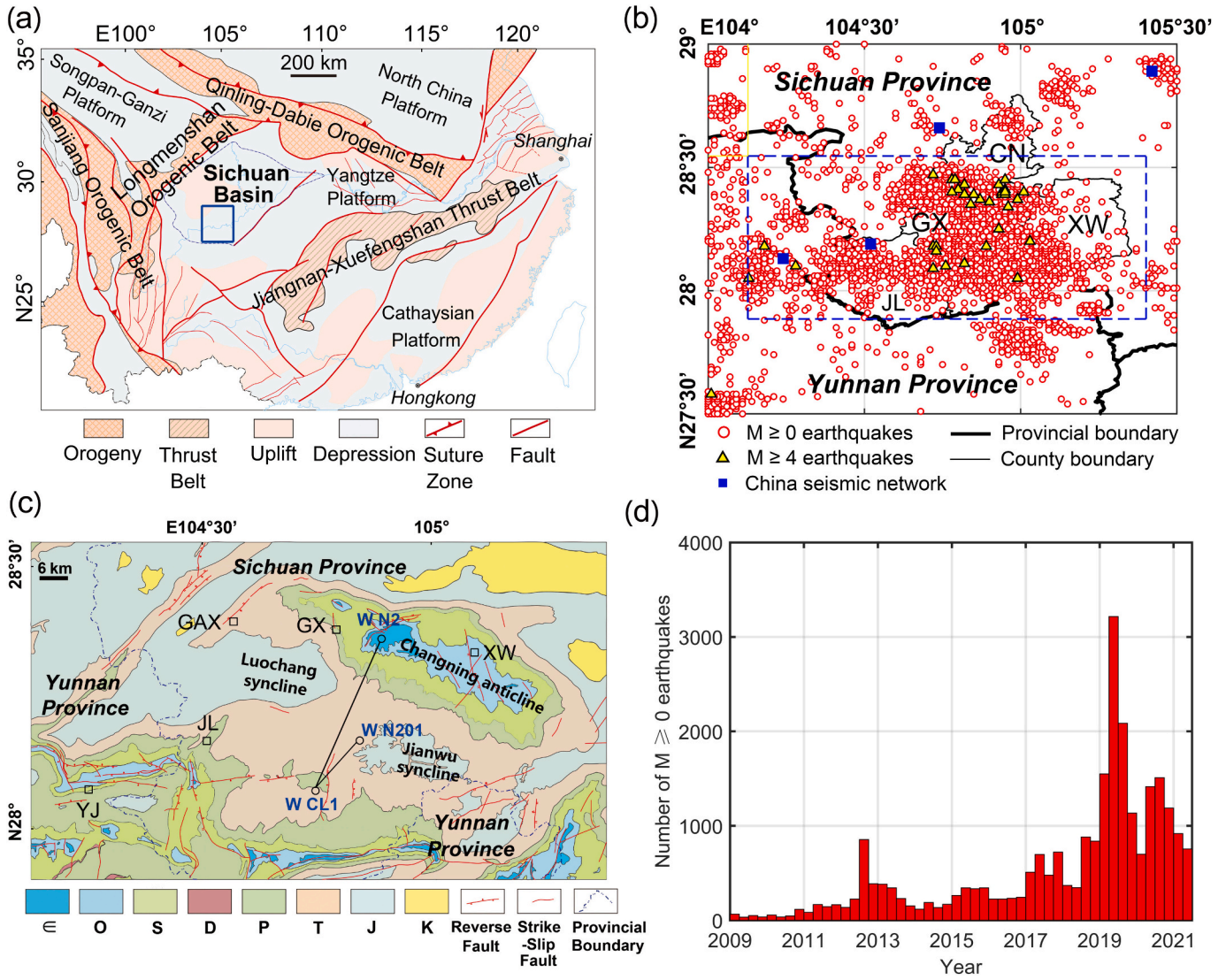

Fig. 1. Seismicity and the geological setting of the Changning Shale Gas Demonstration Block, Sichuan basin, southwest China. (a) Tectonic map of the southern China. The Sichuan Basin is surrounded by the orogenic belts to the north (Qinling-Dabie Orogenic Belt) and west (Longmenshan and Sanjiang Orogenic Belts), and thrust belts to the east (Jiangnan-Xuefengshan Thrust Belt). The blue solid square in Figure (a) refers to the area of Figure (b). (b) Distribution of $M \geq 0.0$ (red circles) and $M \geq 4.0$ (yellow triangles) earthquakes in the Changning Block and adjacent areas (N27.5° to N29° in latitude and E104°to E105.5° in longitude) from January 2009 to June 2021 and depths of 0–10 *km*. The earthquake data are recorded by the regional Chinese national seismic network (blue squares) and retrieved from www.data.earthquake.cn. The Changning Block is defined as the region mainly including the four counties: Changning (CN), Gongxian (GX), Xingwen (XW) and Junlian (JL). The blue dashed square in Figure (b) refers to the area of Figure (c). (c) Geologic structure map of the Changning Block. ∈ = Cambrian, O = Ordovician, S = Silurian, D = Devonian, P = Permian, T = Triassic, J = Jurassic, and K = Cretaceous. GAX = Gaoxian county, YJ = Yanjin county, W N2 = Well N2 (W = Well). (d) The number of $M \geq 0.0$ earthquakes in each quarter year from January 2009 to June 2021 in the Changning Block, with the data shown in Table S2. (For interpretation of the references to colour in this figure legend, the reader is referred to the web version of this article.)

spacing (Meng et al., 2019; Yang et al., 2021). To accurately characterize the regional seismicity in the Changning Block, a two-phased dense seismic array (DSA) with a total of 337 seismic nodal stations and average interstation spacing of 1.5 *km* was deployed (Fig. 2a), covering an area of ~800 km^2 (Yang et al., 2021). The sampling frequency for all the nodal stations was 500 *Hz*, running from 28th February 2019 to 6th May 2019 and representing nearly 70 days. >7500 $M_L \geq 0$ earthquakes (red circles in Fig. 2a-c) were detected between 0 and 10 *km* in depth (mean sea level) with three separate peaks in the distribution identified at different depths (Fig. 2d). According to the geologic sections at three vertical exploration wells (wells N201, CL1 and N2) (Fig. 3), the depth of the first peak corresponds to the lower Silurian Longmaxi Formation – the host unit for the hydraulic fracturing (Xu et al., 2019). The depths of the other two peaks are in the Cambrian-Sinian strata at ~4–6 *km* and below the Longmaxi formation. An important question arises as to how such a multimodal distribution of seismicity can evolve from hydraulic fracturing at shallow depth.

Currently, three potential hypotheses are proposed to address the mechanisms of induced earthquakes associated with fluid injection activities. In the first model, the fault reactivation results from direct fluid injection into the fault, lowering the frictional strength and facilitating fault reactivation (Ellsworth, 2013; Eyre et al., 2019). The second model attributes the fault reactivation to the change in fault loading conditions from the transfer of poroelastic stress (Segall and Lu, 2015; Deng et al., 2016; Bao and Eaton, 2016), and the third model considers that pore pressure-driven aseismic fault slip can reactivate distant faults in the unpressurized regions (Bhattacharya and Viesca, 2019; Cappa et al., 2019; Eyre et al., 2019). While the first model requires a highly permeable path between the reservoir and the fault, the second and third do not. Whether the three individual models or a combination of them can explain the multimodal depth distribution of seismicity remains an open question.

We use outcrop samples of the Cambrian-Sinian sediments (Figs. S1-S4) (present below the producing Longmaxi Formation) to fabricate simulated fault gouge and to explore mechanisms for the multimodal distribution of earthquakes with depths. The Ordovician strata are excluded due to their thin extent. The Cambrian-Sinian strata mainly comprise the Cambrian Xixiangchi-Gaotai-Longwangmiao-Canglangpu-Qiongzhusi Formations and the Sinian the Dengying-Doushantuo Formations (Fig. 3 and Table S1). Shear experiments were performed under hydrothermal conditions corresponding to *in-situ* pressures and temperatures to assess the rheological properties. The resulting rheologies are combined with the multistage hydraulic fracturing model to constrain the anticipated locations and magnitudes of projected poroelastic stress perturbations.

2. Experimental methods

2.1. Gouge preparation

Quantitative analysis of the mineral content was accomplished by X-ray diffraction (XRD) methods according to the standard "Analysis method for clay minerals and ordinary non-clay minerals in sedimentary rocks by X-ray diffraction" (China National Energy Administration, 2018). The procedures for the X-ray diffraction are as follows. First, all rock samples were dried at 50 °*C* for ~12 *h* to remove the moisture. Then, the rocks were crushed and sieved to obtain particle diameters <40 μm. Next, the rock powders were placed within a sealed sample groove and loaded within the X-ray diffractometer (apparatus type: Rigaku D/max-rB) to obtain the diffraction spectrum. Finally, the diffraction data were logged at angles (2θ) between 3° to 70°, a rate of 2°/*min* and intervals of 0.02° at conditions of 100 *mA* and 40 *kV*. The calculation and validation of mineral contents was accomplished following the methods described in Chung (1973) and Moore and Reynolds Jr. (1989). The above procedures were all carried out at the Beidazhihui Micro Structure Analytical Laboratory of Beijing, China. The mineral compositions in each outcrop rock sample from the Xixiangchi through Doushantuo Formations are shown in Fig. 4 and Table S3.

We selected representative rock samples in each formation (Figs. S1-S4) for the simulated fault gouges. Both the Cambrian Xixiangchi and Sinian Dengying Formations contain near-pure dolomite and we selected samples Xxc-7 (97 *wt*% dolomite) and Dy-10 (98 *wt*% dolomite) as representative of the two formations. Many previous studies show that compositionally similar fault gouges are prone to unstable sliding at lower phyllosilicate contents (Takahashi et al., 2007; Tembe et al., 2010; Zhang et al., 2019). The evidence is sourced from not only these laboratory experiments, but also for observations on faults in shale reservoirs and other natural fault zones, such as the San Andreas fault (Carpenter et al., 2009; Kohli and Zoback, 2013; Niemeijer et al., 2010; Passey et al., 2010; Ross and Bustin, 2009). The abundance of phyllosilicate minerals characteristically weakens faults but promotes aseismic sliding, as typified in the San Andreas fault. To evaluate the possibility of unstable sliding, we focus only on samples with the lowest phyllosilicate content in each formation. Thus, samples Gt-3 (10 *wt*% illite and 2 *wt*% chlorite), Lwm-1 (no illite and chlorite), Clp-2 (3 *wt*% illite and 6 *wt*% chlorite), Qzs-4 (4 *wt*% illite and 5 *wt*% chlorite) and Qzs-6 (7 *wt*% illite and 9 *wt*% chlorite) were selected for the friction experiments as representative of the Gaotai, Longwangmiao, Canglangpu and Qiongzhusi Formations. In addition, both the Gaotai and Longwangmiao Formations show the occurrence of thin gypsum layers with low-permeability. We also explore the frictional properties of pure gypsum gouge with generic gypsum samples collected from nearby Tengchong county, Yunnan Province of China. The X-ray diffraction results of the gypsum gouge are shown in Fig. S5 (for particles <75 μm).

2.2. Testing apparatus and procedures

The gouge shear experiments were completed using a high-temperature and high-pressure triaxial shear testing apparatus (He et al., 2006) and a schematic of the apparatus internal structures is shown in Fig. 5. Different from traditional oil-confined triaxial shear apparatuses, this apparatus uses the inert gas (*i.e.*, argon gas) to apply the confining pressure. The maximum applied confining pressure, pore fluid pressure and temperature for this apparatus are 500 *MPa*, 200 *MPa* and 600 °*C*, respectively. The fault driving blocks are 40-*mm*-length and 19.8-*mm*-diameter cylindrical gabbro rocks cut at 35° to the sample axis. The 1-*mm*-thick fault gouges were sandwiched between the two half driving blocks through a precise cylindrical leveling jig. To force the shear to occur within the gouge layers and avoid the boundary shear, the saw-cut surfaces of the gabbro driving blocks were ground and roughened using the 200-mesh carborundum powders. During the shear experiments, the gouge-filled fault driving blocks were inserted into a 0.35-*mm*-thick copper jacket, with cylindrical tungsten carbide and corundum blocks symmetrically placed on both sides. The upper corundum, tungsten carbide and gabbro driving blocks were all drilled with 2-*mm*-diameter boreholes for pore fluid entry (blue channel in Fig. 5). A dense brass filter was placed in the end section of the borehole in the upper gabbro driving block to prevent gouge extrusion into the borehole and to maintain access of the pore fluid. The rubber O-ring seals on both ends of the copper jacket could seal the fault gouge from the confining argon gas. The space between the heating furnace and the copper jacket was uniformly filled with insulating boron nitride powders to prevent gas convection and the fluctuations in confining pressure. The ceramic wool was packed at both ends of the heating furnace to prevent the leakage of boron nitride powders. The high-pressure seal on the upper loading piston maintains the sealing of the whole assembly. The Teflon sheet between the lower loading piston and the copper jacket reduces friction and enhances the sliding of the loading piston.

Before the shear tests, the confining and pore fluid pressures were applied by the (argon) gas pressurization system and the hydraulic pump, respectively. They can be kept constant within ±0.5 *MPa* and ± 0.3 *MPa* respectively by independent servo-controlled intensifiers. As

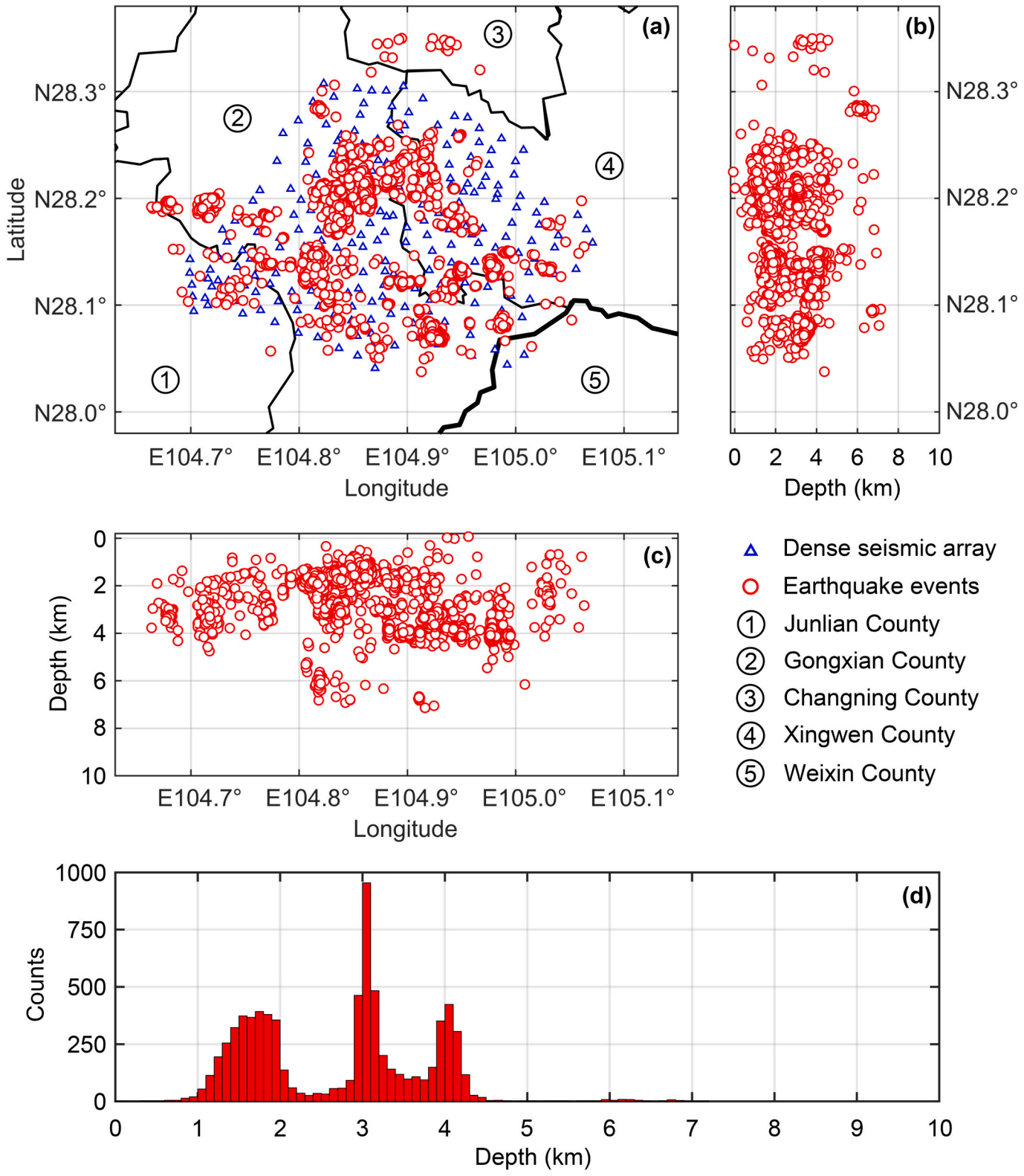

Fig. 2. Seismic events recorded by the dense seismic array in the Changning Shale Gas Demonstration Block deployed from 28th February 2019 to 6th May 2019. (a) Distributions of earthquakes (red circles) from the dense seismic array (blue triangles) in the Changning Block (N27.98°-28.38° in latitude and E104.63°-105.15° in longitude) (Yang et al., 2021). Areas ①, ②, ③, and ④ correspond to the Junlian, Gongxian, Changning and Xingwen counties in the Sichuan province, respectively, with ⑤ identifying Weixin county of Yunnan province. The thin solid lines represent the county boundaries and the thick solid lines the provincial boundaries (Sichuan and Yunnan Provinces). (b) Earthquake depth *versus* latitude. (c) Earthquake depth *versus* longitude. Nucleation depths of the induced events from both the Chinese national seismic network and the dense seismic array are all defined relative to mean sea level. (d) Number of earthquake events *versus* depth. (For interpretation of the references to colour in this figure legend, the reader is referred to the web version of this article.)

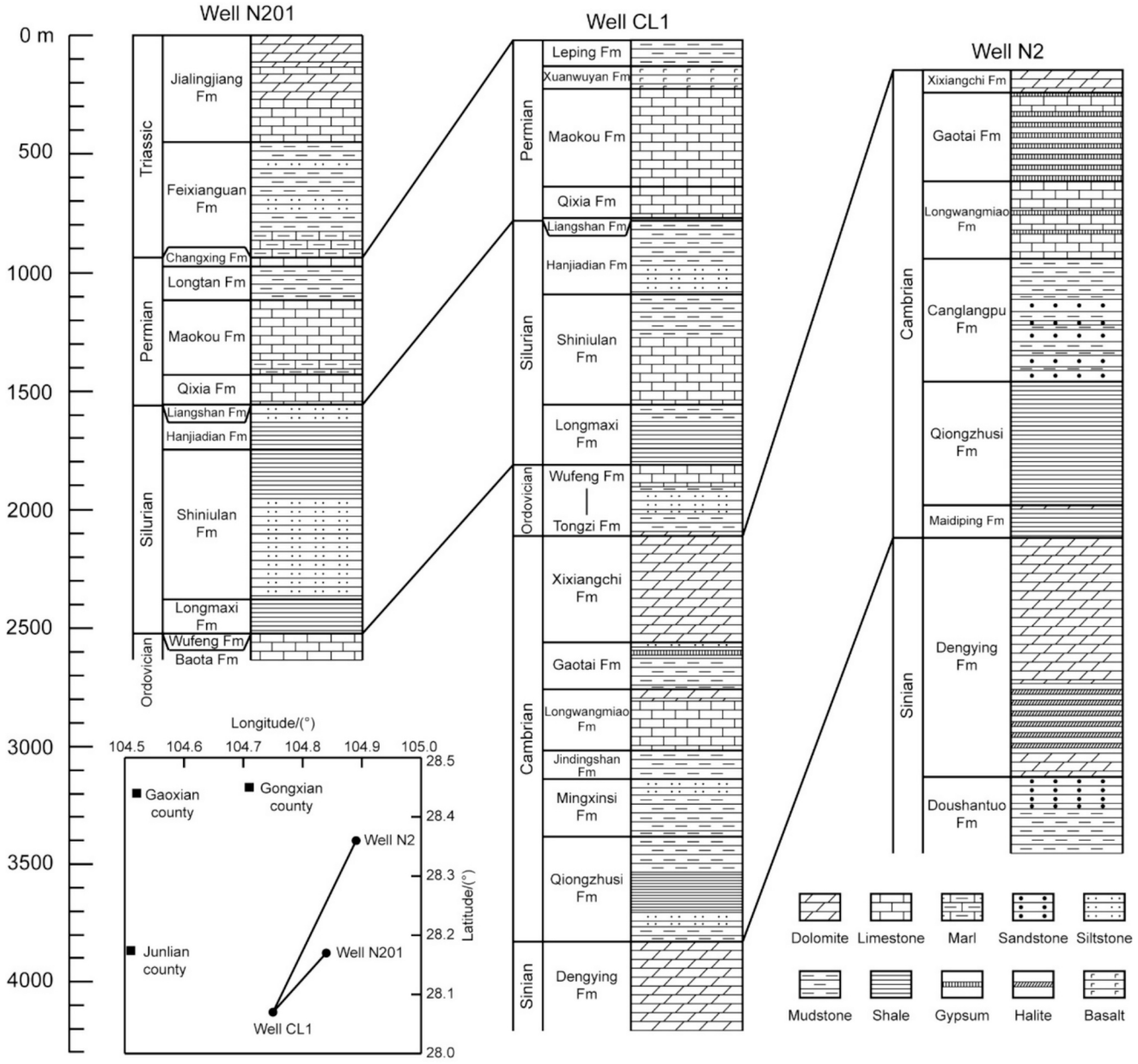

Fig. 3. The geologic sections of three exploration wells (wells N201, CL1 and N2) in Changning Block. The locations of these three wells are denoted in the bottom left insert and Fig. 1c. The top of well N201 is set as the zero baseline depth for comparisons among different sedimentary strata in three wells. Both the Cambrian Jindingshan and Mingxinsi Formations along the well CL1 belong to the Canglangpu Formation.

the air and fluid pressures would increase at elevated temperatures, we initially set the confining pressure and pore fluid pressure to two thirds of the desired values, followed by then elevating the temperature and adjusting the pressures to the final desired values. The temperature was elevated through a two-zone internal furnace. The power of the furnace upper zone is set proportional to the lower zone and thus the applied temperature could be symmetrical along the vertical axis of the sample. During the experiments, the temperature was measured by an independent thermocouple and controlled by a Yamatake-Honeywell DCP30 controller. The measured temperature in this paper all refers to the temperature at the midpoint of the fault gouge zone. At the highest temperature of 600 °*C*, the temperature difference across the fault gouge zone can reach 8 °*C*. The highest applied temperature in our experiments was 180 °*C*, and the temperature difference in the gouge zone should be much <8 °*C*. The temperature could be elevated at a constant rate of 5 °*C*/min with an accuracy of ±2 °*C*. The axial load was applied by the electro-hydraulic servo-control system, and the axial load and displacement were recorded by the load cell and displacement sensor, respectively.

A total of nine shear experiments were carried out at pressures and temperatures corresponding to *in-situ* conditions and the experimental matrix is shown in Table 1. The confining and pore fluid pressures were determined according to the lithostatic pressure (considering a rock density of ~2500 kg/m^3 as representative of the average rock density from these sedimentary layers) and the hydrostatic pressure (assuming fluid density of ~1000 kg/m^3), respectively. Based on Eaton (1975) and Hui et al. (2021), the *in-situ* pore fluid pressure may be estimated from the overburden stress, the hydrostatic pressure and the sonic log data. Regardless, we still employ the hydrostatic pressure to represent the *in-situ* pore fluid pressure as the small fluctuations in static pore fluid pressure are shown to have only a negligible effect on fault frictional strength and stability. The temperature for each experiment was

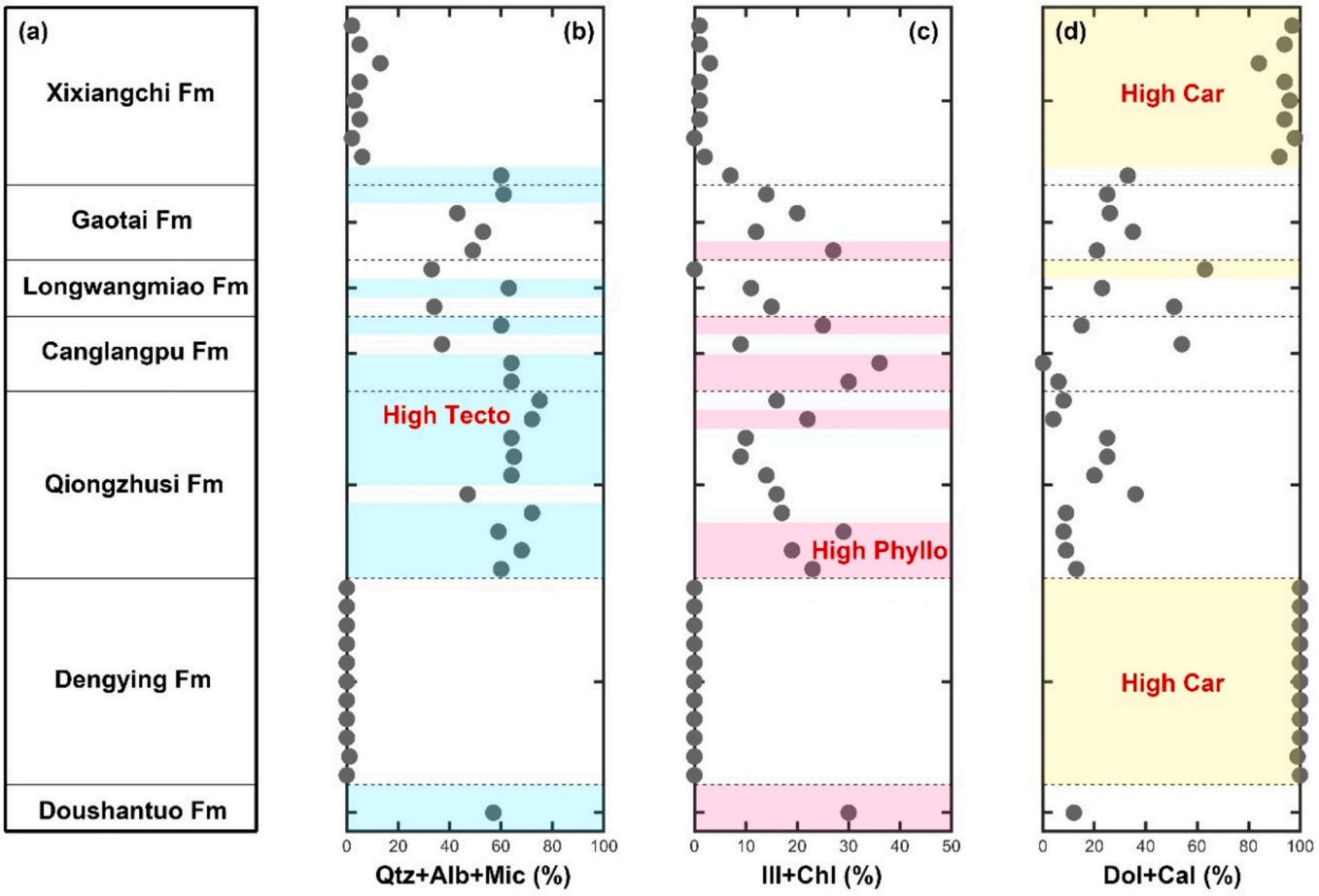

Fig. 4. Mineral compositions of the representative rocks in Upper Cambrian Xixiangchi through Lower Sinian Doushantuo Formations. Qtz = Quartz, Alb = Albite, Mic = Microcline, Ill = Illite, Chl = Chlorite, Dol = Dolomite, Cal = Calcite, Tecto = Tectosilicates, Phyllo = Phyllosilicates, Car = Carbonates. In this paper, the tectosilicates are defined as primarily including quartz, albite and microcline. Phyllosilicates mainly include illite and chlorite, and the dolomite and calcite dominate the carbonates. The cyan, pink and yellow zones represent the high tectosilicate, high phyllosilicate and high carbonate contents, respectively. (For interpretation of the references to colour in this figure legend, the reader is referred to the web version of this article.)

determined based on a temperature gradient of 28 $^{\circ}C/km$ in the Changning Block of Sichuan Basin. Temperatures of 115 $^{\circ}C$ and 150 $^{\circ}C$ represent the upper temperature limits of the Xixiangchi and Qiongzhusi Formations, respectively. Because the gypsum was present both in the Gaotai and Longwangmiao Formations, we conducted shear experiments on the gypsum gouge at a temperature corresponding to the Longwangmiao Formation (120 $^{\circ}C$). The temperatures of 150 $^{\circ}C$ and 180 $^{\circ}C$ are the lower and upper temperature limits for the Dengying Formation. At the beginning of each shear experiment, the fault gouge was sheared at a constant axial loading rate of 1.0 μm/*s* until reaching a steady state friction. To assess the velocity dependence of friction, the axial loading rates were then switched between 1.0, 0.2 and 0.04 μ*m/s*, equivalent to loading velocities of 1.22, 0.244 and 0.0488 μ*m/s* along the shear direction. The shear displacements at the velocities of 1.22 and 0.244 μ*m/s* are 0.366 *mm*, but changes to 0.244 *mm* at a shear velocity of 0.0488 *μm/s*.

2.3. Data analysis

Raw experimental data, including the axial stress (σ_a), axial displacement (l_a), pore fluid pressure (P_f) and temperature (T), were recorded at a sampling frequency of 1 *Hz*. The raw data were corrected for the variation in sample contact area with increasing shear displacement and for shear resistance from the copper jacket. As the confining pressure was applied by the argon gas and not affected by the change of contact area, we only need to correct the axial stress. The relation between the corrected (σ_{ca}) and measured (σ_a) axial stresses is written as,

$$\sigma_{ca} = \frac{\sigma_a}{1 - \frac{2}{\pi}\left[arcsin\frac{\Delta l\tan\alpha}{2r} + \frac{\Delta l\tan\alpha}{2r}\sqrt{1 - \left(\frac{\Delta l\tan\alpha}{2r}\right)^2}\right]} \quad (1)$$

where Δl is the slip along the axial direction, α is the angle of fault driving blocks to the cylinder axis and r is the radius of fault driving blocks. The equivalent shear resistance of the copper jacket was measured by the steel driving blocks with a sandwiched Teflon shim and the friction coefficient between the steel and Teflon shim was tested in another friction testing system (He et al., 2006).

The coefficient of friction μ is calculated as the ratio of the shear stress (τ) and effective normal stress σ_{neff}, expressed as,

$$\mu = \frac{\tau}{\sigma_{neff}} = \frac{\tau}{\sigma_n - P_f} \quad (2)$$

where σ_n and P_f represent the normal stress and pore fluid pressure, respectively.

The velocity dependence of friction is analyzed on the basis of slip rate and state variable constitutive laws (Dieterich, 1979; Marone, 1998; Rice, 1983; Ruina, 1983). The evolution of coefficient of friction is defined as,

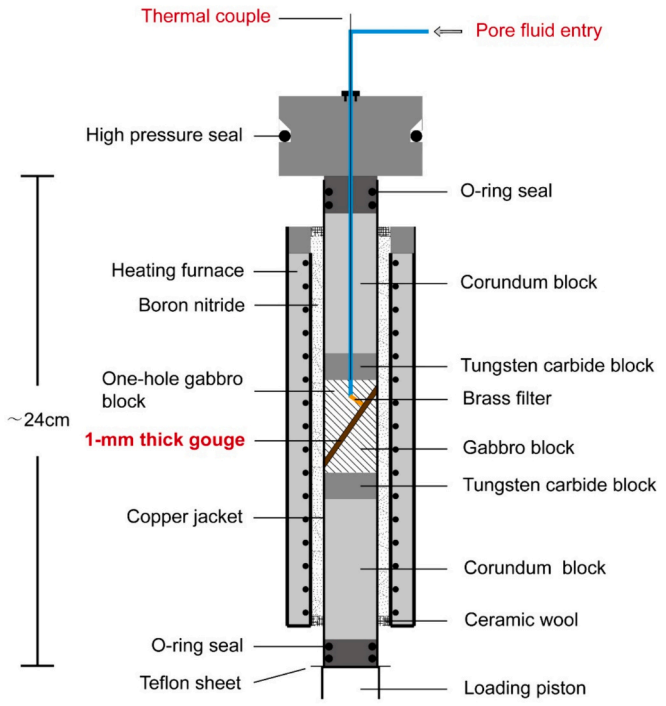

Fig. 5. Schematic of the internal structures of the high-temperature and high-pressure triaxial shear testing apparatus.

$$\mu = \mu_0 + aln\left(\frac{V}{V_0}\right) + bln\left(\frac{V_0\theta}{D_c}\right) \tag{3}$$

$$\frac{d\theta}{dt} = 1 - \frac{V\theta}{D_c} \tag{4}$$

$$\text{or } \frac{d\theta}{dt} = -\frac{V\theta}{D_c} ln\left(\frac{V\theta}{D_c}\right) \tag{5}$$

where μ is the instantaneous coefficient of friction at the shear velocity V, μ_0 is the steady state coefficient of friction at the reference velocity V_0 ($V > V_0$), a and b are empirical constants. a reflects the direct effect from the change of shear velocity, b reflects the evolutional effect of the velocity change, θ is a state variable and describes the average asperity contact lifetime and D_c represents the critical slip necessary to renew the surface contacts. Eqs. (4) and (5) are the Dieterich and Ruina laws that describe the evolution of the state variable θ with time, respectively. At steady state sliding, the state variable θ does not evolve with time and thus $d\theta/dt = 0$. From either Eqs. (3) and (4) or Eqs. (3) and (5), we obtain,

$$a - b = \frac{\Delta\mu_{ss}}{\Delta ln(V)} \tag{6}$$

where $\Delta\mu_{ss}$ denotes the difference in steady-state coefficients of friction before then after a velocity step. Positive values of $(a - b)$ indicate that the steady-state coefficient of friction after the velocity step is larger than that before the velocity step, and are characterized as velocity-strengthening. Faults exhibiting velocity-strengthening behavior will promote inherently stable and aseismic sliding. Conversely, negative values of $(a - b)$ characterize velocity-weakening behavior and facilitate unstable and seismic sliding whenever the critical stiffness is also met (Gu et al., 1984). Examples to determine the magnitudes of $\Delta\mu$ are shown in Fig. S6.

3. Results

A total of nine shear experiments were completed for different combinations of rock gouge composition, confining pressure, pore fluid pressure and temperature in Table 1. The coefficient of friction and shear displacement curves are typical for such gouges, with a near linear increase in friction coefficient initially followed by an inelastic yield point and minor slip hardening (Figs. 6b-6e and 7a-b) or slip weakening (Figs. 6a and 7c-7d) evolution. Most rock gouges deformed as stable shear with only slight stick-slips observed for experiment SICH-3 on gypsum-rich gouge (Fig. 6c). The rock gouges are frictionally strong with frictional strengths mainly within the range 0.6–0.75 (Fig. 8b and Table 2), possibly due to the low phyllosilicate contents and high contents of tectosilicates or carbonates. The gouges in experiments SICH-1 (from the Xixiangchi Formation) and in SICH-8 and SICH-9 (from the Dengying Formation) are mostly pure dolomite with the coefficient of friction for the dolomite gouges decreasing slightly from ~0.697 at $T = 115\ ^\circ C$, to ~0.646 at $T = 150\ ^\circ C$ and ~ 0.616 at $T = 180\ ^\circ C$ (Fig. 8b and Table 2). Compared with the results for dolomite gouge under hydrothermal conditions from Scuderi et al. (2013a) and Pluymakers et al. (2016), the frictional strengths of dolomite gouge are influenced by the magnitudes of both effective normal stress and temperature (Table S4). The trends of frictional strength with temperature for the dolomite gouge is in accordance with these prior results (Scuderi et al., 2013b; Pluymakers et al., 2016) (Table S4) as well.

Results of velocity-stepping experiments to evaluate frictional stability $(a - b)$ are summarized in Fig. 8c and Table 2. The rock gouges exhibit a range of behaviors from velocity-strengthening in the Xixiangchi ($a - b = 0.0041$ to 0.0096) and Gaotai ($a - b = 0.0020$ to 0.0029) Formations, to velocity-neutral in the Longwangmiao ($a - b = -0.0011$ to 0.0014), Canglangpu ($a - b = -0.0001$ to 0.0008) and Qiongzhusi ($a - b = -0.0002$ to 0.0021) Formations, and apparent velocity-weakening in the Dengying Formation ($a - b = -0.0029$ to 0.0155) (Table 2). For the dolomite gouges from the Xixiangchi or Dengying Formations, frictional stability $(a - b)$ evolves from 0.0041 to 0.0096 at $T = 115\ ^\circ C$, to −0.0021 to 0.0155 at $T = 150\ ^\circ C$ and − 0.0029 to 0.0112 at $T = 180\ ^\circ C$, implying that instability in favored at higher temperatures or in deeper strata (Table 2). Our results are consistent with previous studies on the frictional stability of dolomite gouge (Fig. 8d). The dolomite gouges characterized in Pluymakers et al. (2016) and Scuderi et al. (2013a)

Table 1
Testing conditions. The thickness of each formation is determined from the three exploration wells in Fig. 3. The corresponding thicknesses of Xixiangchi, Gaotai, Longwangmiao, Canglangpu, Qiongzhusi, Maidiping, Dengying, and Doushantuo Formations are 0.45 *km*, 0.20 *km*, 0.25 *km*, 0.35 *km*, 0.45 *km*, 0.15 *km*, 1.00 *km*, and 0.35 *km*, respectively. σ_c = confining pressure, P_f = pore fluid pressure, T = temperature.

Testing Number	Simulated gouge	Formation	σ_c (*MPa*)	P_f (*MPa*)	T (°*C*)	Corresponding depth
SICH-1	Xxc-7	Xixiangchi	80	30	115	2.80–3.25 *km*
SICH-2	Gt-3	Gaotai	85	30	115	3.25–3.45 *km*
SICH-3	Gypsum	–	85	30	120	3.30–3.50 *km*
SICH-4	Lwm-1	Longwangmiao	90	35	120	3.45–3.70 *km*
SICH-5	Clp-2	Canglangpu	95	35	130	3.70–4.05 *km*
SICH-6	Qzs-4	Qiongzhusi	100	40	150	4.05–4.50 *km*
SICH-7	Qzs-6	Qiongzhusi	100	40	150	4.05–4.50 *km*
SICH-8	Dy-10	Dengying	120	50	150	4.65–5.65 *km*
SICH-9	Dy-10	Dengying	120	50	180	4.65–5.65 *km*

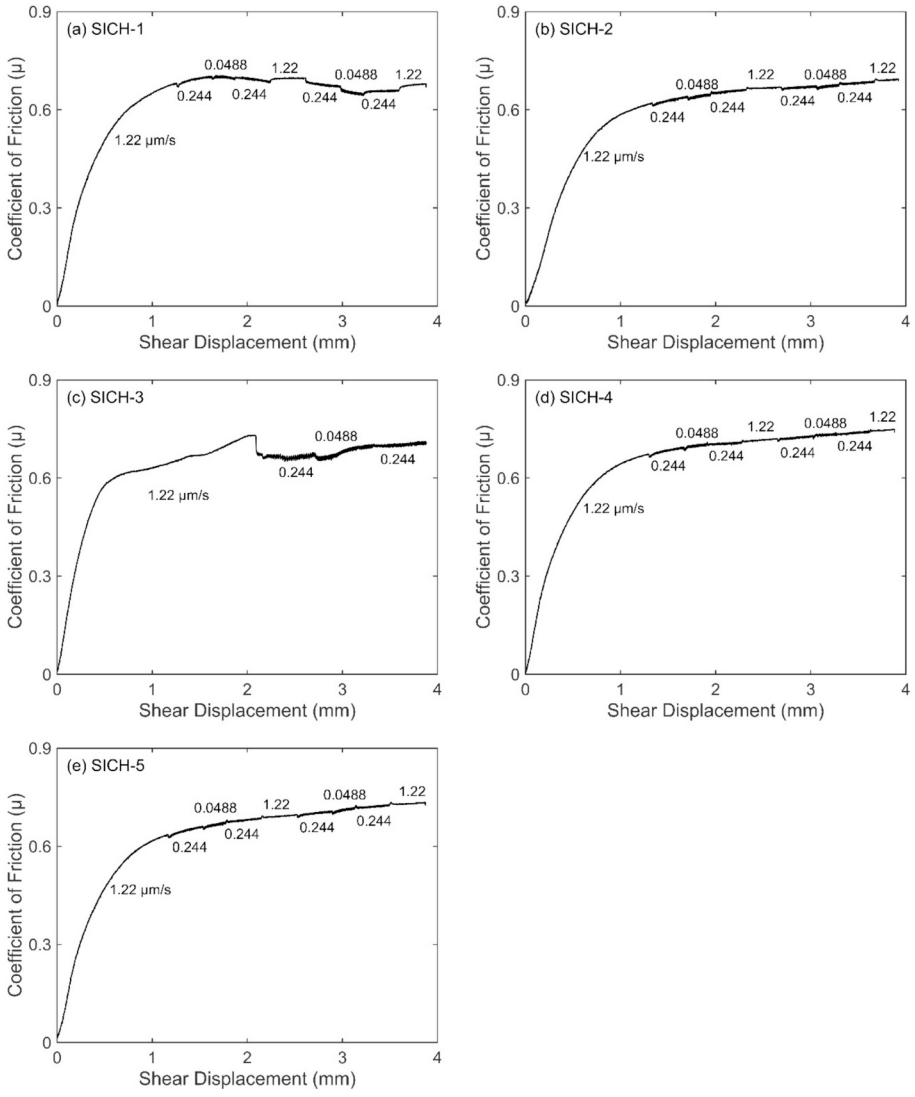

Fig. 6. Relationship of the coefficient of friction and the shear displacement for different experiments, (a) SICH-1, (b) SICH-2, (c) SICH-3, (d) SICH-4, and (e) SICH-5. The shear velocities are marked around the curves.

exhibit a transition from velocity-strengthening to velocity-weakening behaviors at $T \approx 120\ ^{\circ}C$ when dry, but at $T \approx 150\ ^{\circ}C$ when wet. The frictional stability also shows a strong dependence on the shear velocity, especially at $T = 150$ and $180\ ^{\circ}C$. The values of $(a - b)$ for the dolomite gouge at shear velocities of 0.244–0.0488 or 0.0488–0.244 μm/*s* all indicate velocity-weakening behaviors, but evolve to strong velocity-strengthening behaviors at shear velocities of 1.22–0.244 and 0.244–1.22 μ*m/s* (Fig. 8c and Table 2). As an important interlayer within the Gaotai through Longwangmiao Formations, the gypsum gouge also shows slight velocity-weakening behavior at faster velocities of 1.22–0.244 and 0.244–1.22 *μm/s*. This indicates that the gypsum gouge may be a factor in promoting fault instability in either of these (Gaotai or Longwangmiao) Formations.

4. Discussion

4.1. Mechanisms of multimodal earthquake distribution

Based on our previous studies on the frictional and stability properties of the Longmaxi shale gouges under the hydrothermal conditions (An et al., 2020a), the Longmaxi shale gouges show a decrease in carbonate content (from ~80 *wt*% to 0%) and an increase in tectosilicate content (from ~10 *wt*% to ~80 *wt*%) from the top (close to the Silurian Shiniulan Formation) to the base (close to the Ordovician Wufeng Formation) of the formation. Most of the Longmaxi shale gouges show inherently stable and aseismic responses and only ~5% are brittle shales (with phyllosilicates <20 *wt*%) that exhibit potentially unstable and seismic responses. Elevating the pore fluid pressure to simulate the high fluid pressure encountered during hydraulic fracturing also retains the frictionally stable response of the Longmaxi shale gouges at *in-situ* temperatures of ~90 *°C* (Scuderi and Collettini, 2018; An et al., 2020b). Although the ~5% of brittle shale faults could be reactivated and induce seismicity during hydraulic fracturing, the frequency of seismicity should be small, due to their limited presence. Considering that the first peak in the distribution of seismicity with depth is within the zone pressurized by hydraulic fracturing, we speculate that the instantaneous stress drops on pre-existing faults that results from direct fluid injection and the related reduction in effective normal stress could account for the swarms of earthquakes detected by the dense seismic array (Fig. 2).

The experimental data in Fig. 8 indicate that the Cambrian-Sinian strata contain brittle faults that may promote unstable and seismic slip at *in-situ* pressures and temperature, especially for the Cambrian Xixiangchi and Sinian Dengying Formations that contain thick and pure (dry/wet) dolomite. Combined with our previous numerical modeling results that demonstrate that the changes in the Coulomb failure stress (ΔCFS) exceed 10^{-2} *MPa* at distances of <4.0 *km* (An et al., 2021), the

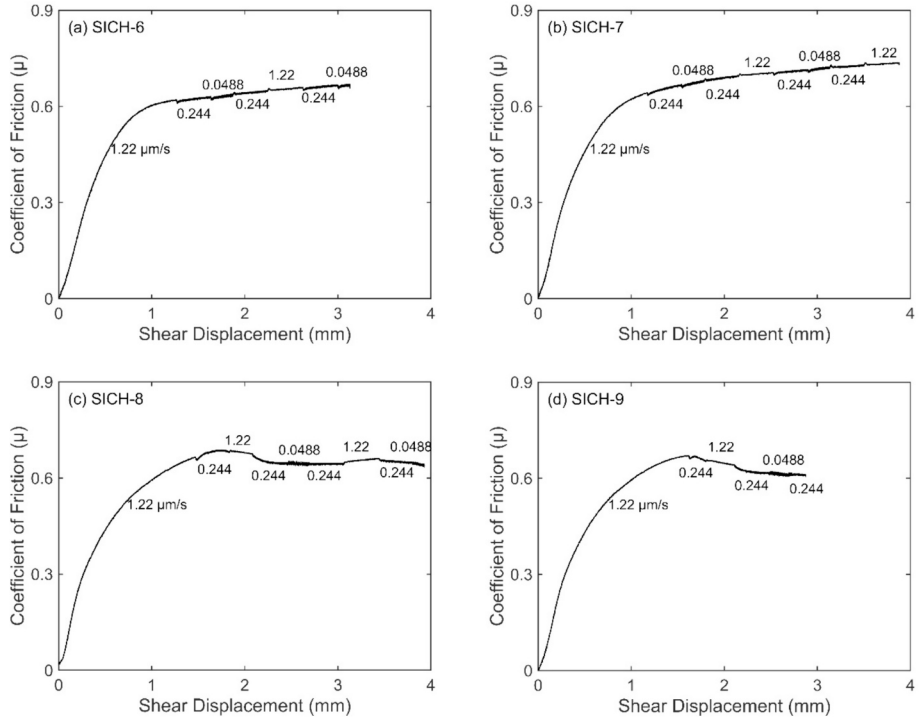

Fig. 7. Relationship of the coefficient of friction and the shear displacement for different experiments, (a) SICH-6, (b) SICH-7, (c) SICH-8, and (d) SICH-9.

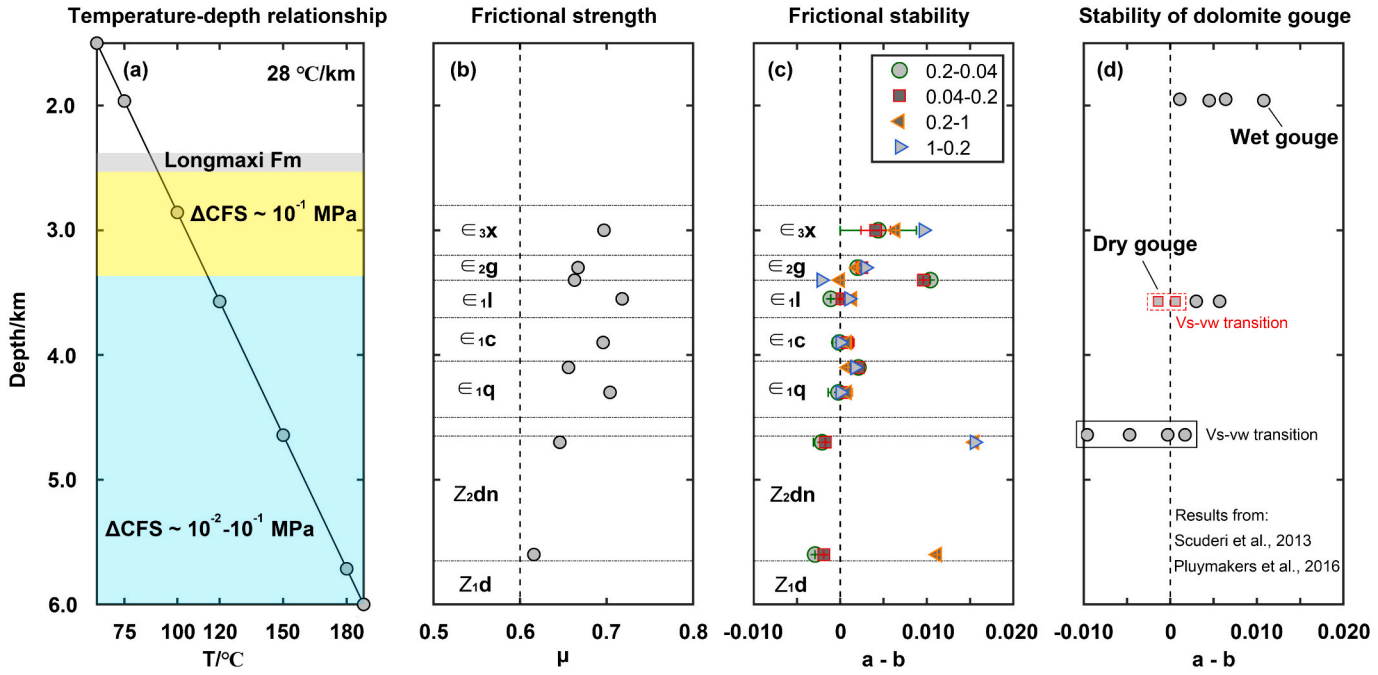

Fig. 8. Frictional characteristics of rock gouges from the Xixiangchi through Dengying Formations at hydrothermal conditions. (a) Relationship between temperature and depth in the Changning Block representing an average temperature gradient of 28 °*C/km*. The gray rectangle shows the depth range of the Longmaxi Formation. The yellow and cyan zones indicate that the changes in Coulomb failure stress (*ΔCFS*) are in the respective magnitude range of 10^{-1} *MPa* and 10^{-2}–10^{-1} *MPa* respectively and these results are derived from our previous research (An et al., 2021). (b) The frictional strength of rock gouges from the Xixiangchi through Dengying Formations. $\in_3$x = Xixiangchi, $\in_2$g = Gaotai, $\in_1$l = Longwangmiao, $\in_1$c = Canglangpu, $\in_1$q = Qiongzhusi, Z_2dn = Dengying, and Z_1d = Doushantuo Formations. (c) Frictional stability of rock gouges from the Xixiangchi through Dengying Formations. Positive values of (a – b) imply that the fault gouge will fail aseismically, while negative values of (a – b) indicate the potential for unstable slip. (d) As the Xixiangchi and Dengying Formations both contain thick and nearly-pure layers of dolomite, the frictional properties of dolomite gouge from previous studies are used for comparison (Scuderi et al., 2013a; Pluymakers et al., 2016). (For interpretation of the references to colour in this figure legend, the reader is referred to the web version of this article.)

Table 2
Experimental results. l_{final} = final shear displacement, μ = coefficient of friction. The coefficients of friction in most experiments were obtained at a shear displacement of 2.5 *mm* and a shear velocity of 1.22 μm/*s*, except for experiments SICH-3 (at $V = 0.244$ μm/*s*), SICH-8 (at $V = 0.0488$ μm/*s*) and SICH-9 (at $V = 0.0488$ μm/*s*) due to the slip-weakening responses in friction. The errors in values of $(a - b)$ are standard deviations from the same velocity steps in each test. The first velocity step was excluded in the calculation of $(a - b)$ for all experiments to ensure that the data are qualified in their steady states.

Testing Number	l_{final} (*mm*)	μ	$(a - b)$ at shear velocities of			
			0.244–0.0488 μm/*s*	0.0488–0.244 μm/*s*	0.244–1.22 μm/*s*	1.22–0.244 μm/*s*
SICH-1	3.88	0.697	0.0044 ± 0.0044	0.0041 ± 0.0017	0.0064	0.0096
SICH-2	3.92	0.667	0.0020 ± 0.0001	0.0025 ± 0.0003	0.0020 ± 0.0001	0.0029
SICH-3	3.88	0.663	0.0104	0.0096	0	−0.0022
SICH-4	3.88	0.718	−0.0011	0.0002 ± 0.0002	0.0014 ± 0.0003	0.0010
SICH-5	3.87	0.696	−0.0001 ± 0.0008	0.0008 ± 0.0008	0.0008 ± 0.0004	0
SICH-6	3.13	0.656	0.0021	0.0021	0.0009	0.0017
SICH-7	3.88	0.704	−0.0002 ± 0.0012	0.0005 ± 0.0009	0.0008 ± 0.0006	0
SICH-8	3.93	0.646	−0.0021 ± 0.0010	−0.0017	0.0155	0.0155
SICH-9	2.88	0.616	−0.0029	−0.0019	0.0112	–

stress perturbations from multistage hydraulic fracturing can reactivate critically-stressed faults and trigger the seismicity in the Cambrian-Sinian strata. This can partially explain the multimodal depth distribution of seismicity below the hydraulic fracturing zone. Although we assume the largest feasible fracture aperture in our calculation for the one well pad, this corresponds to the most dangerous case. Our previous simulation model (An et al., 2021) followed the typical well configuration of the Changning area with the background consistent with the current study. The hydraulic fracturing was performed in the Longmaxi formation at a burial depth of ~2.5 *km* where the elastic modulus (E) and Poisson's ratio (ν) are the average values representative of these sedimentary layers. As separation distance from the injection well is the most important factor that defines the magnitude of ΔCFS, and then changes in mechanical properties at the same distance/location would exert little effect on the magnitude of the ΔCFS. Thus, our calculated $\Delta CFSs$ are broadly applicable. The stress perturbations from the simultaneous hydraulic fracturing from multiple well pads could be more destabilizing than those obtained in this study of a single well pad. In addition, according to the third model considered here for mechanisms of induced seismicity (Bhattacharya and Viesca, 2019; Cappa et al., 2019; Eyre et al., 2019), fluid-pressure-driven aseismic slip in the pressurized zones could also trigger earthquakes in the adjacent Cambrian-Sinian strata that contain brittle earthquake-prone rocks. From Fig. 1b, the magnitudes of >30 earthquakes are close to or higher than M_L 4.0 necessitating slip on an area of at least 1 km^2 (Zoback and Gorelick, 2012). In the Changning Block, the thicknesses of the Cambrian Xixiangchi and Qiongzhusi Formations are larger than 500 *m* and the thickness of the Sinian Dengying Formation is larger than 1000 *m* (Xu et al., 2019), all sufficient to host such large fault ruptures.

4.2. Implications for injection-induced earthquakes

Our experimental combined with the previous modeling results have important implications in understanding mechanisms contributing to the observed multimodal depth distribution of seismicity encountered during hydraulic fracturing in the Changning Block. As depicted in Fig. 9, the natural faults are prone to nucleate seismicity at higher temperatures and pressures with prior natural earthquakes mainly occurring at a greater depth. Fluid injection may significantly elevate local pore fluid pressures and contribute to the swarms of observed

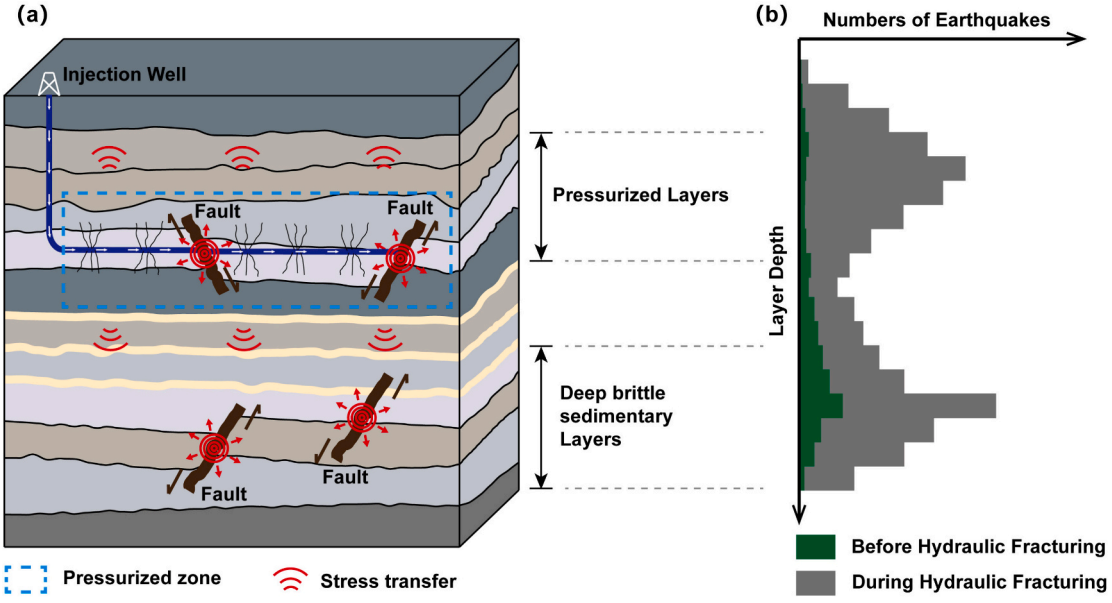

Fig. 9. Mechanisms implicated in the multimodal depth distribution of seismicity resulting from shallow hydraulic fracturing. (a) Schematic representation of hydraulic fracturing injection in the shallow reservoir layer and fault responses. The blue dashed square indicates the pressurized zones by hydraulic fracturing. Red radiating symbols show the transmission of poroelastic stresses. Hydraulic fracturing induced fluid pressures directly reactivate proximal faults within the reservoir but propagating poroelastic stresses reactivate critically-stressed faults both distally within the reservoir at depth where no hydraulic communication exists. (b) Distribution of earthquakes with depth. Colors represent the distinct depth distributions of earthquakes both before (green) and during (gray) hydraulic fracturing operations. (For interpretation of the references to colour in this figure legend, the reader is referred to the web version of this article.)

earthquakes in the shallow reservoir and pressurized zones. Stress perturbations from multistage hydraulic fracturing are shown capable of reactivating critically-stressed faults in the deep brittle sedimentary strata that containing earthquake-prone rocks. Pore fluid pressure-driven aseismic fault slip within the reservoir layer could also trigger the response of disconnected and hydraulically isolated faults in the deeper brittle sedimentary strata. Our results therefore imply that all three potential modes of triggering of injection-induced earthquakes are feasible in contributing to the observed multimodal depth distribution of seismicity within Changning Block – either individually or collectively.

5. Conclusions

Direct fluid injection into the gas-bearing Longmaxi shale in the Sichuan basin may significantly reduce effective stresses and promote fault failure that contributes to the swarms of earthquakes in and around that shallow reservoir. However, this does not explain the evolution of seismic events at significantly greater depth in the underlying strata that evolve simultaneously with the periods of fluid injection. Rather, our friction-stability experiments on the underlying Cambrian through Sinian rocks gouges at conditions corresponding to *in-situ* pressures and temperatures reveal that the strata below the hydraulic fracturing zones contain earthquake-prone rocks and favor reactivation of seismic faulting. Numerical modeling to define the poroelastic stress perturbations resulting from multistage hydraulic fracturing in the higher strata indicates that the magnitudes of the changes in Coulomb failure stress (ΔCFS) at depth are higher than the 10^{-2} *MPa* broadly recognized *as* sufficient to reactivate critically-stressed faults. The combined experimental and modeling results together can explain the mechanisms nucleating remote earthquakes in the deeper brittle sedimentary strata that underlay the injection zone – as by direct fluid access and by poroelastic stress transfer. Our results demonstrate that both direct fluid injection and poroelastic stress transfer from multistage hydraulic fracturing are feasible causal mechanisms contributing to the multimodal distribution of seismicity with depth in the Changning Block. And that the triggered events remain within the sedimentary pile rather than within the underlying basement.

CRediT authorship contribution statement

Mengke An: Writing – original draft, Funding acquisition, Formal analysis, Conceptualization. **Derek Elsworth:** Writing – review & editing, Validation, Conceptualization. **Fengshou Zhang:** Writing – review & editing. **Rui Huang:** Writing – review & editing, Validation, Data curation. **Junlun Li:** Writing – review & editing. **Zhengyu Xu:** Writing – review & editing. **Zhen Zhong:** Writing – review & editing. **Manchao He:** Writing – review & editing.

Declaration of competing interest

The authors declare that they have no known competing financial interests or personal relationships that could have appeared to influence the work reported in this paper.

Data availability

Data will be made available on request.

Acknowledgements

This research is funded by the National Natural Science Foundation of China (42107163, 42320104003), and the Fundamental Research Funds for the Central Universities. DE acknowledges support from the G. Albert Shoemaker endowment. We thank Wenming Yao and Jianye Chen for laboratory assistance. The experimental data in this paper can be found at Doi: https://doi.org/10.5061/dryad.cvdncjt9p.

Appendix A. Supplementary data

Supplementary data to this article can be found online at https://doi.org/10.1016/j.tecto.2024.230332.

References

An, M., Zhang, F., Elsworth, D., Xu, Z., Chen, Z., Zhang, L., 2020a. Friction of Longmaxi shale gouges and implications for seismicity during hydraulic fracturing. J. Geophys. Res. Solid Earth 125 (8), e2020JB019885. https://doi.org/10.1029/2020JB019885.

An, M., Zhang, F., Chen, Z., Elsworth, D., Zhang, L., 2020b. Temperature and fluid pressurization effects on frictional stability of shale faults reactivated by hydraulic fracturing in the Changning block, Southwest China. J. Geophys. Res. Solid Earth 125 (8), e2020JB019584. https://doi.org/10.1029/2020JB019584.

An, M., Zhang, F., Dontsov, E., Elsworth, D., Zhu, H., Zhao, L., 2021. Stress perturbation caused by multistage hydraulic fracturing: Implications for deep fault reactivation. Int. J. Rock Mech. Min. Sci. 141, 104704 https://doi.org/10.1016/j.ijrmms.2021.104704.

Atkinson, G.M., Eaton, D.W., Igonin, N., 2020. Developments in understanding seismicity triggered by hydraulic fracturing. Nat. Rev. Earth Environ. 1, 264–277. https://doi.org/10.1038/s43017-020-0049-7.

Bao, X., Eaton, D.W., 2016. Fault activation by hydraulic fracturing in western Canada. Science 354 (6318), 1406–1409. https://doi.org/10.1126/science.aag2583.

Bhattacharya, P., Viesca, R.C., 2019. Fluid-induced aseismic fault slip outpaces pore-fluid migration. Science 364 (6439), 464–468. https://doi.org/10.1126/science.aaw7354.

Cappa, F., Scuderi, M.M., Collettini, C., Guglielmi, Y., Avouac, J.P., 2019. Stabilization of fault slip by fluid injection in the laboratory and in situ. Sci. Adv. 5, eaau4065. https://doi.org/10.1126/sciadv.aau4065.

Carpenter, B.M., Marone, C., Saffer, D.M., 2009. Frictional behavior of materials in the 3D SAFOD volume. Geophys. Res. Lett. 36 (5) https://doi.org/10.1029/2008GL036660.

China National Energy Administration, 2018. Analysis method for clay minerals and ordinary non-clay minerals in sedimentary rocks by the X-ray diffraction. SY/T, 5163–2018, 1-44.

Chung, F.H., 1973. Quantitative interpretation of X-ray diffraction patterns of mixtures. I. Matrix-flushing method for quantitative multicomponent analysis. J. Appl. Crystallogr. 7 (6), 519–525. https://doi.org/10.1107/S0021889874010375.

Deng, K., Liu, Y., Harrington, R.M., 2016. Poroelastic stress triggering of the December 2013 crooked Lake, Alberta, induced seismicity sequence. Geophys. Res. Lett. 43, 8482–8491. https://doi.org/10.1002/2016GL070421.

Dieterich, J.H., 1979. Modeling of rock friction: 1. Experimental results and constitutive equations. J. Geophys. Res. 84 (B5), 2161. https://doi.org/10.1029/JB084iB05p02161.

Eaton, B.A., 1975. The equation for geopressure prediction from well logs. In: Paper presented at the Fall Meeting of the Society of Petroleum Engineers of AIME, Dallas, Texas, September 1975. https://doi.org/10.2118/5544-MS.

Ellsworth, W.L., 2013. Injection-induced earthquakes. Science 341, 142–149. https://doi.org/10.1126/science.1225942.

Elsworth, D., Spiers, C.J., Niemeijer, A.R., 2016. Understanding induced seismicity. Science 354 (6318), 1380–1381. https://doi.org/10.1126/science.aal2584.

Eyre, T.S., Eaton, D.W., Garagash, D.I., Zecevic, M., Venieri, M., Weir, R., Lawton, D.C., 2019. The role of aseismic slip in hydraulic fracturing-induced seismicity. Sci. Adv. 5, eaav7172. https://doi.org/10.1126/sciadv.aav7172.

Grigoli, F., Cesca, S., Rinaldi, A.P., Manconi, A., López-Comino, J.A., Clinton, J.F., Westaway, R., Cauzzi, C., Dahm, T., Wiemer, S., 2018. The November 2017 M_w 5.5 Pohang earthquake: a possible case of induced seismicity in South Korea. Science 360 (6392), 1003–1006. https://doi.org/10.1126/science.aat2010.

Gu, J.C., Rice, J.R., Ruina, A.L., Tse, S.T., 1984. Slip motion and stability of a single degree of freedom elastic system with rate and state friction. J. Mech. Phys. Solids 32 (3), 167–196. https://doi.org/10.1016/0022-5096(84)90007-3.

He, C., Yao, W., Wang, Z., Zhou, Y., 2006. Strength and stability of frictional sliding of gabbro gouge at elevated temperatures. Tectonophysics 427 (1–4), 217–229. https://doi.org/10.1016/j.tecto.2006.05.023.

Hui, G., Chen, S., Chen, Z., He, Y., Wang, S., Gu, F., 2021. Investigation on two M_w 3.6 and M_w 4.1 earthquakes triggered by poroelastic effects of hydraulic fracturing operations near Crooked Lake, Alberta. J. Geophys. Res. Solid Earth 126 (5), e2020JB020308. https://doi.org/10.1029/2020JB020308.

Kohli, A.H., Zoback, M.D., 2013. Frictional properties of shale reservoir rocks. J. Geophys. Res. Solid Earth 118, 5109–5125. https://doi.org/10.1002/jgrb.50346.

Kolawole, F., Johnston, C., Morgan, B.C., Chang, J., Carpenter, B., 2019. The susceptibility of Oklahoma's basement to seismic reactivation. Nat. Geosci. 12 (10), 839–844. https://doi.org/10.1038/s41561-019-0440-5.

Lei, X., Huang, D., Su, J., Jiang, G., Wang, X., Wang, H., Guo, X., Fu, H., 2017. Fault reactivation and earthquakes with magnitudes of up to M_w 4.7 induced by shale-gas hydraulic fracturing in Sichuan Basin, China. Sci. Rep. 7, 7971. https://doi.org/10.1038/s41598-017-08557-y.

Lei, X., Wang, Z., Su, J., 2019. The December 2018 M_L 5.7 and January 2019 M_L 5.3 earthquakes in South Sichuan Basin induced by shale gas hydraulic fracturing. Seismol. Res. Lett. 90, 1099–1110. https://doi.org/10.1785/0220190182.

Liu, J., Zahradník, J., 2020. The 2019 M_w 5.7 Changning earthquake, Sichuan Basin, China: a shallow doublet with different faulting styles. Geophys. Res. Lett. 47, e85408 https://doi.org/10.1029/2019GL085408.

Majer, E.L., Baria, R., Stark, M., Oates, S., Bommer, J., Smith, B., Asanuma, H., 2007. Induced seismicity associated with Enhanced Geothermal Systems. Geothermics 36, 185–222. https://doi.org/10.1016/j.geothermics.2007.03.003.

Marone, C., 1998. Laboratory-derived friction laws and their application to seismic faulting. Annu. Rev. Earth Planet. Sci. 26 (1), 643–696. https://doi.org/10.1146/annurev.earth.26.1.643.

Meng, L., McGarr, A., Zhou, L., Zang, Y., 2019. An investigation of seismicity induced by hydraulic fracturing in the Sichuan basin of China based on data from a temporary seismic network. Bull. Seismol. Soc. Am. 109, 348–357. https://doi.org/10.1785/0120180310.

Moein, M.J.A., Langenbruch, C., Schultz, R., Grigoli, F., Ellsworth, W.L., Wang, R., et al., 2023. The physical mechanisms of induced earthquakes. Nat. Rev. Earth Environ. 4, 847–863. https://doi.org/10.1038/s43017-023-00497-8.

Moore, D.M., Reynolds Jr., R.C., 1989. X-Ray Diffraction and the Identification and Analysis of Clay Minerals. Oxford University Press (OUP), Oxford.

Niemeijer, A., Marone, C., Elsworth, D., 2010. Fabric induced weakness of tectonic faults. Geophys. Res. Lett. 37, L03304. https://doi.org/10.1029/2009GL041689.

Passey, Q.R., Bohacs, K.M., Esch, W.L., Klimentidis, R., Sinha, S., 2010. From oil-prone source rock to gas-producing shale reservoir—Geologic and petrophysical characterization of unconventional shale-gas reservoirs. In: Paper presented at the CPS/SPE International Oil & Gas Conference and Exhibition, Beijing, China, 8–10 June 2010. https://doi.org/10.2118/131350-MS.

Pluymakers, A., Niemeijer, A.R., Spiers, C.J., 2016. Frictional properties of simulated anhydrite-dolomite fault gouge and implications for seismogenic potential. J. Struct. Geol. 84, 31–46. https://doi.org/10.1016/j.jsg.2015.11.008.

Qiu, Z., Zou, C., Wang, H., Dong, D., Wei, L., 2020. Discussion on the characteristics and controlling factors of differential enrichment of shale gas in the Wufeng-Longmaxi Formations in South China. J. Nat. Gas Geosci. 5 (3), 117–128. https://doi.org/10.1016/j.jnggs.2020.05.004.

Rice, J.R., 1983. Constitutive relations for fault slip and earthquake instabilities. PAGEOPH 121 (3), 443–475. https://doi.org/10.1007/BF02590151.

Ross, D.J.K., Bustin, R.M., 2009. The importance of shale composition and pore structure upon gas storage potential of shale gas reservoirs. Mar. Pet. Geol. 26 (6), 916–927. https://doi.org/10.1016/j.marpetgeo.2008.06.004.

Ruina, A., 1983. Slip instability and state variable friction laws. J. Geophys. Res. Solid Earth 88 (B12), 10359–10370. https://doi.org/10.1029/JB088iB12p10359.

Scuderi, M.M., Collettini, C., 2018. Fluid injection and the mechanics of frictional stability of shale-bearing faults. J. Geophys. Res. Solid Earth 123, 8364–8384. https://doi.org/10.1029/2018JB016084.

Scuderi, M.M., Niemeijer, A.R., Collettini, C., Marone, C., 2013a. Frictional properties and slip stability of active faults within carbonate-evaporite sequences: the role of dolomite and anhydrite. Earth Planet. Sci. Lett. 369-370, 220–232. https://doi.org/10.1016/j.epsl.2013.03.024.

Scuderi, M.M., Niemeijer, A.R., Collettini, C., Marone, C., 2013b. Frictional properties and slip stability of active faults within carbonate-evaporite sequences: the role of dolomite and anhydrite. Earth Planet. Sci. Lett. 369-370, 220–232. https://doi.org/10.1016/j.epsl.2013.03.024.

Segall, P., Lu, S., 2015. Injection-induced seismicity: Poroelastic and earthquake nucleation effects. J. Geophys. Res. Solid Earth 120, 5082–5103. https://doi.org/10.1002/2015JB012060.

Shapiro, S.A., Dinske, C., Rothert, E., 2006. Hydraulic-fracturing controlled dynamics of microseismic clouds. Geophys. Res. Lett. 33 https://doi.org/10.1029/2006GL026365.

Takahashi, M., Mizoguchi, K., Kitamura, K., Masuda, K., 2007. Effects of clay content on the frictional strength and fluid transport property of faults. J. Geophys. Res. 112, B08206. https://doi.org/10.1029/2006JB004678.

Tembe, S., Lockner, D.A., Wong, T.-F., 2010. Effect of clay content and mineralogy on frictional sliding behavior of simulated gouges: Binary and ternary mixtures of quartz, illite, and montmorillonite. J. Geophys. Res. 115, B03416. https://doi.org/10.1029/2009JB006383.

Walsh, F.R., Zoback, M.D., 2015. Oklahoma's recent earthquakes and saltwater disposal. Sci. Adv. 1 (5), 1–9. https://doi.org/10.1126/sciadv.1500195.

Xu, Z., Jiang, S., Yao, G., Liang, X., Xiong, S., 2019. Tectonic and depositional setting of the lower Cambrian and lower Silurian marine shales in the Yangtze Platform, South China: Implications for shale gas exploration and production. J. Asian Earth Sci. 170, 1–19. https://doi.org/10.1016/j.jseaes.2018.10.023.

Yang, W., Chen, G.Y., Meng, L.Y., Zang, Y., Li, J.L., 2021. Determination of the local magnitudes of small earthquakes using a dense seismic array in the Changning-Zhaotong shale gas field, southern Sichuan Basin. Earth Planet. Phys. 5 (3), 1–15. https://doi.org/10.26464/epp2021026.

Zhang, F., An, M., Zhang, L., Fang, Y., Elsworth, D., 2019. The role of mineral composition on the frictional and stability properties of powdered reservoir rocks. J. Geophys. Res. Solid Earth 124, 1480–1497. https://doi.org/10.1029/2018JB016174.

Zoback, M.D., Gorelick, S.M., 2012. Earthquake triggering and large-scale geologic storage of carbon dioxide. Proc. Natl. Acad. Sci. 109 (26), 10164–10168. https://doi.org/10.1073/pnas.1202473109.

Zou, C., Guo, J., Jia, A., Wei, Y., Yan, H., Jia, C., Tang, H., 2020. Connotations of scientific development of giant gas fields in China. Nat. Gas Industry B 7 (5), 533–546. https://doi.org/10.1016/j.ngib.2020.09.011.